Powering the Kingdom's Energy Grid with Sodium-Ion Batteries through Electrolyte Engineering

Fayruz Yar
Mentor: Dr. Wandi Wahyudi
Principal Investigator: Prof. Husam Alshareef
King Abdullah University for Science and Technology (KAUST)

Fayruz.yar@kaust.edu.sa, Wandi.wahyudi@kaust.edu.sa, husam.alshareef@kaust.edu.sa

Abstract

Sodium-ion batteries (SIBs) are promising candidates for large-scale energy storage because of the abundance and low cost of sodium. However, electrolyte-derived interfacial instability and irreversible sodium loss remain important challenges, particularly in hard-carbon||$Na_4Fe_3(PO_4)_2P_2O_7$ (HC||NFPP) full cells. In this work, a 1 M $NaPF_6$/diglyme (G2) electrolyte was evaluated with 1 wt% tris(trimethylsilyl) phosphate (TMSPa), tris(2,2,2-trifluoroethyl) borate (TTFPB), and thiophene-2-carbonitrile (TPC), as well as selected mixed-additive formulations. The effects of the additives on the electrolyte solvation environment were investigated using liquid-state ^{1}H and ^{23}Na nuclear magnetic resonance (NMR) spectroscopy, while the structural evolution of HC and NFPP electrodes was examined using X-ray diffraction (XRD). Electrochemical performance was evaluated in Na||HC and Na||NFPP half cells and in HC||NFPP full cells. All additives modified the average sodium coordination environment, with TTFPB producing the largest apparent change in the ^{23}Na resonance. However, the electrochemical results showed that solvation changes did not directly translate into improved full-cell performance. TPC caused substantial irreversible sodium consumption, resulting in an initial Coulombic efficiency (ICE) of only 50% and severe capacity fading in the full cell. The TPC/TTFPB mixture performed even worse, with ICE of 34%. In contrast, 1 wt% TMSPa achieved ICE of 86%, identical to that of the baseline electrolyte (BE), and maintained a capacity close to the baseline after 100 cycles. Nevertheless, the additive-free 1 M $NaPF_6$/G2 electrolyte remained the most stable formulation under the tested conditions. XRD confirmed the retention of the main structural features of both HC and NFPP during cycling. Overall, the results demonstrate that electrolyte-additive selection for HC||NFPP SIBs should be guided by full-cell sodium balance and long-term interfacial stability rather than by half-cell capacity or solvation changes alone.

Table of Contents

1. Introduction **4**

2. Methodology **8**

2.1 Chemicals and Preparation **8**

2.1.1 Electrode Preparation 8

2.1.2 Separator drying and cell assembly 8

2.1.3 Electrolyte and Electrolyte Additives 8

2.2 Characterizations **8**

2.2.1 Nuclear Magnetic Resonance (NMR) 8

2.2.2 X-ray diffraction (XRD) 9

2.3 Electrochemical Investigation of NaPF6/G2-Based Sodium-Ion Cells **9**

3. Results and Discussion **9**

3.1 Characterizations Results **9**

3.1.1 NMR Spectra 9

3.1.2 XRD Pattern 10

3.2 Electrochemical Investigation of NaPF6/G2-Based Sodium-Ion Cells **11**

4. Conclusion **14**

ACKNOWLEDGEMENT **15**

References **15**

Table of Figures

Figure 1 Crystal structure of NFPP cathode. 5
Figure 2 Hard carbon structure. 5
Figure 3 Diglyme chemical structure 6
Figure 4 TMSPa chemical structure. 7
Figure 5 TTFPB chemical structure. 7
Figure 6 TPC chemical structure. 7
Figure 7 (a) ^{1}H and (b) ^{23}Na NMR spectra of $NaPF_6$-G2 with 1 wt% TPC, TTFPB, or TMSPa. 10
Figure 8 XRD patterns of (a) HC and (b) NFPP electrodes extracted from HC‖NFPP full cells at different charge and discharge voltages. 11
Figure 9 (a) Charge-Discharge profile and (b) discharge capacity and efficiency of HC half-cell. 12
Figure 10 (a) Charge-Discharge profile and (b) discharge capacity and efficiency of NFPP half-cell. 13
Figure 11 (a) Charge-Discharge profile and (b) discharge capacity and efficiency of HC||NFPP. 14
Figure 12 (a) Charge-Discharge profile and (b) discharge capacity and efficiency of HC||NFPP at different temperatures. 14

1. Introduction

Global energy consumption continues to rise, driven by population growth, industrialization, and expanding access to electricity across developing regions. Fossil fuels still supply the majority o this demand, but their combustion releases large quantities of carbon dioxide and other greenhouse gases, contributing to global warming, ocean acidification, and air quality degradation [1]. Beyond these environmental costs, fossil resources are finite and geographically concentrated, exposing energy markets to price volatility and geopolitical risk. Together, these pressures have made the transition toward cleaner, more sustainable energy sources an urgent global priority.

Renewable energy technologies, including solar and wind offer an attractive alternative. They are virtually inexhaustible, emit little to no greenhouse gases during operation, and their costs fallen sharply over the past decade, making them increasingly competitive with conventional generation. However, renewable output is inherently intermittent and weather dependent, and generation does not necessarily coincide with periods of peak demand. This mismatch between supply and demand limits the share of renewables that can be reliably integrated into existing grids without additional infrastructure.

Energy storage has emerged as the key enabling technology for resolving this mismatch, allowing surplus renewable generation to be captured and dispatched when needed [2]. Several storage technologies have been developed for this purpose, including pumped hydroelectric storage, compressed air energy storage, flywheels, and supercapacitors [3]. Pumped hydro and compressed air systems, while mature and capable of storing large amounts of energy, are constrained by strict geographical and geological requirements and involve substantial capital investment [4]. Flywheels and supercapacitors offer fast response and high-power density but store comparatively little energy and are prone to self-discharge, making them unsuitable for sustained, long-duration storage [5]. On the other hand, electrochemical batteries combine reasonably high energy density with high round-trip efficiency, flexible siting independent of geography, and scalability from portable devices to grid-scale installations [6].

Among battery chemistries, lithium-ion batteries (LIBs) have dominated the market since their commercialization, owing to their high energy and power density, long cycle life, and a mature, well-established manufacturing infrastructure. Despite these advantages, LIBs face growing challenges. Lithium reserves are geographically concentrated in a small number of regions, and rising demand has led to price volatility and supply chain concerns. Many high-performance lithium cathodes additionally rely on cobalt and nickel, raising both cost and ethical sourcing concerns, while flammable organic electrolytes pose ongoing safety risks related to thermal runaway [7]. These limitations have motivated the search for alternative battery chemistries built on more abundant and evenly distributed resources.

Sodium-ion batteries (SIBs) have emerged as one of the most promising “beyond-lithium” alternatives. Sodium is far more abundant than lithium and is distributed globally rather than concentrated in a handful of regions, giving SIBs an inherent cost and supply-security advantage. SIBs operate on the same “rocking-chair” intercalation principle as LIBs, allowing much of the existing lithium-ion manufacturing infrastructure to be adapted with relatively minor modification. An additional practical benefit is that, unlike lithium, sodium does not alloy with aluminum at low potential, allowing aluminum current collectors to replace copper on the anode side as well as the cathode side, further reducing cost and cell weight.
The performance of a sodium-ion battery is governed largely by its cathode, anode, and electrolyte.

Several cathode families have been explored for SIBs, including layered transition-metal oxides (NaxMO2), Prussian blue analogues, and polyanionic compounds such as phosphates, pyrophosphates, and fluorophosphates [6]. Among these, Na4Fe3(PO4)2P2O7 (NFPP), a mixed phosphate–pyrophosphate compound, has attracted particular attention. As shown in **Figure 1**, its large diffusion channels support efficient sodium ion (Na^+) transport, and the structure undergoes negligible volume change (<4%) during cycling, giving it excellent structural stability and long cycle life [8]. Because NFPP is iron-based rather than vanadium-based,

it avoids the cost and toxicity concerns associated with vanadium-containing analogues, while still delivering a stable, two-plateau voltage profile around 3.2 and 2.9 V vs. Na/Na^+ and a theoretical capacity of approximately 129 mAh g^{-1}. This balance of low cost, environmental compatibility, and cycling stability makes NFPP one of the most practical cathode candidates for large-scale SIBs deployment.

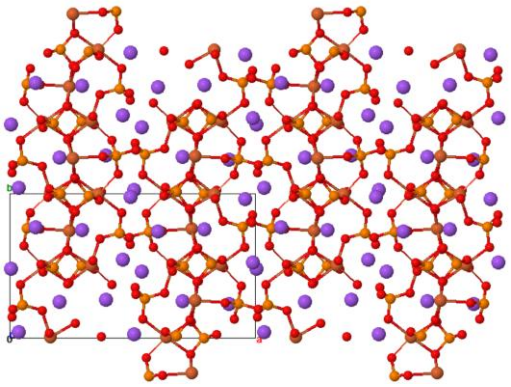


Figure 1 Crystal structure of NFPP cathode.

On the anode side, graphite, the standard choice for LIBs, performs poorly in sodium-ion systems, as intercalation of Na^+ between graphite layers is thermodynamically unfavorable [9]. This has driven interest in alternative anode materials, including alloy-type compounds and hard carbon (HC) [10]. Alloy-type anodes offer high theoretical capacity but undergo large volume expansion during cycling, leading to mechanical degradation and poor cycling stability [11]. HC (**Figure 2**), a disordered, non-graphitizable carbon with a turbostratic microstructure, has instead become the benchmark SIB anode. Sodium storage in hard carbon proceeds through a combination of surface/defect adsorption, intercalation between graphitic domains, and pore-filling within closed nanopores, giving it a low, largely flat working potential close to that of sodium plating [12]. Combined with its low cost and compatibility with abundant, often biomass-derived precursors, HC offers an attractive balance of capacity, voltage profile, and economic viability, which explains its widespread adoption in SIB research and development.



Figure 2 Hard carbon structure.

Despite this progress at the electrode level, sodium-ion batteries still face several limitations relative to their lithium-ion counterparts [13]. The larger ionic radius and atomic mass of Na^+ compared with Li^+ result in intrinsically lower gravimetric and volumetric energy density and slower solid-state diffusion kinetics in many electrode materials. Perhaps more critically, the solid electrolyte interphase (SEI) and cathode electrolyte interphase (CEI) layers formed in sodium systems tend to be less uniform and less stable than their lithium-ion

analogues, since SEI-forming chemistry optimized for LIB electrolytes does not translate directly to sodium chemistry [14]. This interfacial instability manifests as continuous electrolyte decomposition, capacity fade, and low initial coulombic efficiency -particularly at the hard carbon anode- and represents one of the principal bottlenecks currently limiting the practical cycle life of SIBs [15].

Because many of these limitations originate at the electrode–electrolyte interface, electrolyte engineering is a direct and cost-effective approach for improving SIB performance. The electrolyte must simultaneously provide sufficient ionic conductivity, stable sodium salt dissociation, chemical compatibility with both electrodes, and a sufficiently wide electrochemical stability window. In addition, it strongly influences the composition, thickness, and stability of the SEI on HC and the CEI on the NFPP cathode [17].

In this study, 1 M sodium hexafluorophosphate ($NaPF_6$) dissolved in diglyme (G2) was selected as the baseline electrolyte. $NaPF_6$ is commonly used in sodium-ion batteries because it provides high ionic conductivity and good solubility in aprotic organic solvents. However, PF_6^- containing salts are sensitive to trace moisture and may undergo hydrolysis, producing acidic and fluorinated species that can promote electrolyte degradation and damage electrode interphases. This issue is particularly important at elevated temperature, where salt decomposition and parasitic interfacial reactions are expected to accelerate.

Diglyme, shown in **Figure 3**, is a glyme-based ether solvent with a relatively low viscosity and strong Na^+ coordination ability. Ether electrolytes can provide fast Na^+ transport and favorable desolvation kinetics, and they are often associated with lower first-cycle irreversible capacity loss than carbonate-based electrolytes. Diglyme-based electrolytes have also shown promising compatibility with hard-carbon electrodes. However, ether electrolytes may be vulnerable to oxidative decomposition at high cathode potentials and can still form unstable interphases depending on the electrode surface, salt chemistry, temperature, and applied voltage window. Therefore, although $NaPF_6$/G2 provides a suitable baseline electrolyte for HC-based sodium-ion cells, further interfacial stabilization is required for long-term HC||NFPP full-cell cycling. Diglyme electrolytes have been reported to offer a relatively wide operating window and low initial loss in selected sodium-ion systems, but their performance can remain limited by interfacial instability and capacity retention in HC-based full cells.

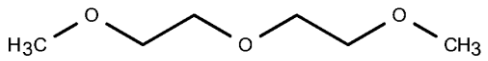


Figure 3 Diglyme chemical structure

To regulate the electrode–electrolyte interfaces, three structurally different additives were investigated: tris(trimethylsilyl) phosphate (TMSPa), tris(2,2,2-trifluoroethyl) borate (TTFPB), and 2-thiophenecarbonitrile (TPC). TMSPa (**Figure 4**) contains phosphate and trimethylsilyl groups. The Si-containing groups can scavenge moisture-derived and fluoride-containing reactive species through formation of strong Si–F bonds, thereby reducing electrolyte acidification and suppressing further salt decomposition. TMSPa has also been reported to influence interfacial chemistry and reduce impedance growth in related battery systems.

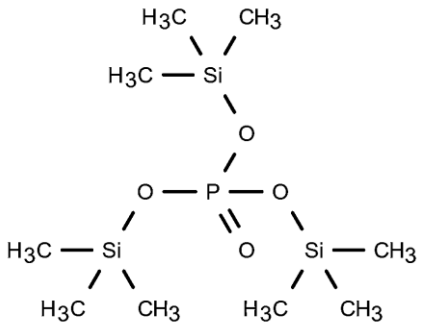


Figure 4 TMSPa chemical structure.

TTFPB (**Figure 5**) is a fluorinated borate ester. Its electron-deficient boron centre can interact with anionic electrolyte species, while its fluorinated groups may promote formation of boron- and fluorine-containing interphase components. Such chemistry may be beneficial for CEI stabilization. However, its effect is highly dependent on electrode chemistry, salt, solvent, additive concentration, and the operating voltage range.

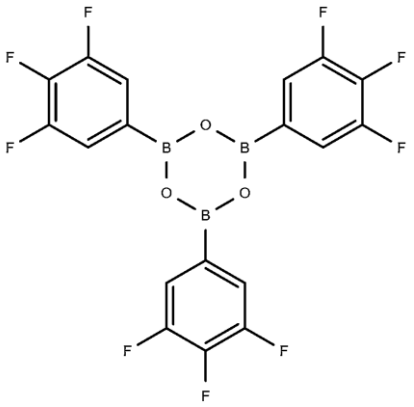


Figure 5 TTFPB chemical structure.

TPC (**Figure 6**) contains fluorinated aromatic groups and boron–oxygen functionality. Its molecular structure suggests that it may be electrochemically reactive and could participate information of fluorine- and boron-containing interphase products. The role of TPC was therefore investigated experimentally rather than assumed a priori.

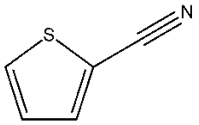


Figure 6 TPC chemical structure.

Accordingly, this work investigates the individual and combined effects of TPC, TMSPa, and TTFPB in a 1 M $NaPF_6$/G2 electrolyte for NFPP||HC sodium-ion batteries. The additives were evaluated in Na||HC and Na||NFPP half cells, followed by HC||NFPP full cells, to assess their influence on first-cycle Coulombic efficiency, capacity, and interfacial stability. The temperature dependence of the baseline full-cell was additionally examined at room temperature and 60°C. Through this stepwise comparison, the study examines whether half-cell performance can reliably predict full-cell behavior and identifies the most promising electrolyte formulation under the tested conditions.

2. Methodology

2.1 Chemicals and Preparation

2.1.1 Electrode Preparation

Hard-carbon (HC) electrodes were prepared from a slurry containing 90 wt% HC, 5 wt% Super P conductive carbon, and 5 wt% poly(vinylidene fluoride) (PVDF) binder dispersed in N-methyl-2-pyrrolidone (NMP). NFPP electrodes were prepared using 80 wt% NFPP active material, 10 wt% Super P, and 10 wt% PVDF in NMP. The slurries were centrifuged to remove trapped air bubbles and to improve slurry homogeneity before coating. The HC and NFPP slurries were coated onto carbon-coated aluminium foil current collectors and dried in a vacuum oven at 80°Covernight. The dried electrode sheets were punched into circular discs with a diameter of 16 mm. The punched electrodes were subsequently dried again in a vacuum oven at 80°Covernight to remove residual NMP and moisture before transfer to an Ar-filled glovebox.

2.1.2 Separator drying and cell assembly

Glass-fibre separators were punched into 16 mm discs and dried in a vacuum oven at 80°Covernight prior to use. The dried electrodes and separators were transferred to an Ar-filled glovebox for cell assembly. CR2032-type coin cells were assembled using the prepared HC and NFPP electrodes, a glass-fibre separator, and the corresponding electrolyte. Stainless-steel spacers and springs were included to maintain mechanical pressure and electrical contact within the cell. The cells were sealed using a coin-cell crimping machine.

2.1.3 Electrolyte and Electrolyte Additives

Sodium hexafluorophosphate (NaPF_6) and diglyme (G2) were used as the sodium salt and solvent, respectively, to prepare the baseline electrolyte (BE). The BE consisted of 1 M NaPF_6 dissolved in G2. All electrolyte components were stored and handled under an inert atmosphere (argon gas) to minimize exposure to moisture. Three electrolyte additives were investigated: thiop-2-carbonitrile (TPC), tris(2,2,2-trifluoroethyl) borate (TTFPB), and tris(trimethylsilyl) phosphate (TMSPa). All the electrolyte additives were used as received. For the individual-additive electrolytes, each additive was introduced at 1 wt% relative to the total electrolyte mass. The formulations were denoted as 1 wt% TPC, 1 wt% TTFPB, and 1 wt% TMSPa. Mixed-additive electrolytes containing 0.5 wt% TPC + 0.5 wt% TMSPa and 0.5 wt% TPC + 0.5 wt% TTFPB were also prepared, giving a total additive content of 1 wt% in each formulation. The electrolyte solutions were stirred until homogeneous before cell assembly.

2.2 Characterizations

2.2.1 Nuclear Magnetic Resonance (NMR)

Liquid-state ^{1}H and ^{23}Na NMR spectroscopy were used to investigate the effect of electrolyte additives on the solvation environment of $NaPF_6$in diglyme (G2). The baseline electrolyte, consisting of 1 M NaPF_6 in G2, and electrolyte formulations containing 1 wt% TPC, TTFPB, or TMSPa were analyzed under identical conditions. The electrolyte samples were loaded into the outer compartment of coaxial NMR tubes. A sealed inner capillary containing 0.1 M NaPF_6 dissolved in DMSO-d_6 was used as an external reference and lock for the ^{1}H and ^{23}Na NMR measurements. The spectra were recorded using Bruker NMR spectrometer at room temperature. The resulting spectra were processed and compared according to their chemical shifts and line shapes.

2.2.2 X-ray diffraction (XRD)

XRD measurements were performed to investigate the structural evolution of HC and NFPP electrodes during charge and discharge of HC||NFPP full cells. Full cells containing the baseline electrolyte, 1 M NaPF_6 in G2, were stopped at selected cell voltages during the first cycle. The cells were disassembled, and the HC and NFPP electrodes were collected separately for XRD analysis. The electrode states examined included the pristine electrodes, electrodes extracted after charging to 2.8 and 3.4 V, and electrodes extracted after discharging to 2.6 and 1.5 V. The XRD patterns were compared to monitor changes in the broad turbostratic diffraction features of HC and the crystalline diffraction features of NFPP during sodium insertion and extraction. Measurements were performed using a D8 Bruker diffractometer with Cu Kα radiation over a 2θrange of 5-80°.

2.3 Electrochemical Investigation of NaPF_6/G2-Based Sodium-Ion Cells

The electrochemical behavior of the baseline 1 M NaPF_6/G2 electrolyte and its additive-containing formulations was evaluated in sodium-ion coin cells. The baseline electrolyte was first examined in Na||HC and Na||NFPP half cells, as well as HC||NFPP full cells, to establish its compatibility with both electrodes and its full-cell cycling behavior. The effect of elevated temperature was subsequently evaluated by cycling the baseline HC||NFPP full cell at room temperature and 60°C. Finally, the influence of TPC, TTFPB, TMSPa, and selected mixed-additive formulations on the electrochemical response was compared using the same cell configurations.

3. Results and Discussion

3.1 Characterizations Results

3.1.1 NMR Spectra

The ^1H NMR spectrum (**Figure 7a**) of the baseline electrolyte, 1 M NaPF_6 G2, is dominated by the resonances of diglyme. Three main proton environments are observed in the range of approximately 3.20–3.50 ppm. The signal at around 3.20 ppm is assigned to the terminal methoxy protons, $-OCH_3$, while the signals between approximately 3.35–3.40 ppm and 3.45–3.49 ppm originate from the two non-equivalent methylene proton environments of the ether backbone, $-CH_2OCH_2$ −and $-OCH_2CH_2OCH_3$. The exact positions and line shapes differ from those of neat diglyme because G2 molecules coordinate to Na^+through their ether oxygen atoms in the NaPF_6/G2 electrolyte. Reference spectra of diglyme likewise show three principal proton environments associated with terminal $-OCH_3$ and two ether-adjacent $-CH_2$ −groups. After addition of 1 wt% TPC, TTFPB, and TMSPa, the same three G2-derived resonance regions are retained. This confirms that the additives do not change the fundamental molecular identity of diglyme. However, the peaks display additive-dependent differences in chemical shift, line width, and fine structure, especially in the methylene regions around 3.35–3.40 and 3.45–3.49 ppm. Since these protons are close to the ether oxygen atoms that coordinate Na^+, these spectral changes indicate that the additives perturb the local G2 coordination environment. The changes may result from altered Na^+–G2 interactions, modified association between $Na^+$and PF_6^-, or both.

The ^{23}Na NMR spectra (**Figure 7b**) provide a complementary view of the same solvation behavior. The baseline electrolyte displays one broad sodium resonance, consistent with fast exchange among different sodium-containing environments in solution. These can include G2-solvated Na^+, solvent-separated ion pairs, contact ion pairs, and potentially larger aggregates. Therefore, the observed chemical shift represents a population-weighted average rather than a separate signal for each species. Relative to BE, all additives modify the position and/or line shape of the ^{23}Na resonance, confirming additive-dependent changes in the average sodium coordination environment. TTFPB gives the largest apparent displacement of the sodium resonance,

while TPC and TMSPa also produce detectable changes. Thus, the three additives affect the NaPF_6/G2 solvation network to different extents.

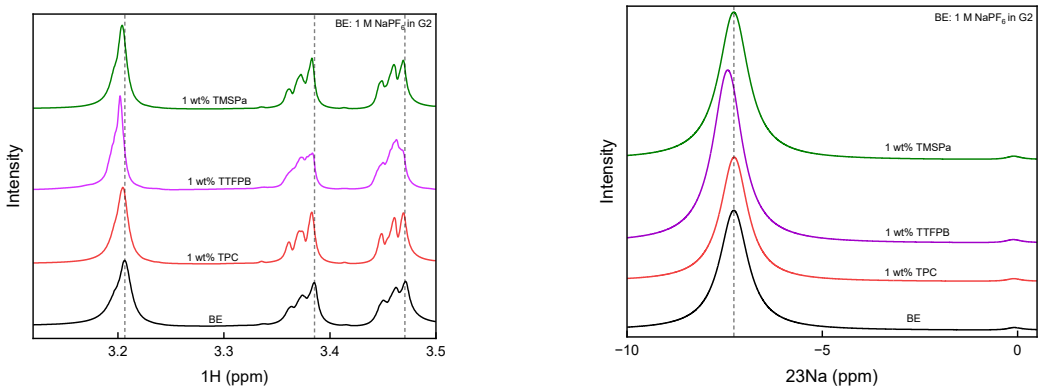


Figure 7 (a) ^{1}H and (b) ^{23}Na NMR spectra of $NaPF_6$-G2 with 1 wt% TPC, TTFPB, or TMSPa.

3.1.2 XRD Pattern

Ex situ XRD was conducted on the hard-carbon and NFPP electrodes extracted from the HC||NFPP full cell at selected states of charge and discharge (**Figure 8**). During charging of the full cell to 2.8 and 3.4 V, Na^+ ions were transferred from NFPP to HC. Therefore, HC underwent progressive sodiation, while NFPP underwent progressive desodiation. During discharge to 2.6 and 1.5 V, the reverse process occurred, with Na^+ returning from HC to NFPP.

Based on **Figure 8a**, the HC patterns exhibit broad diffraction features characteristic of a disordered turbostratic carbon structure. These features are retained at all investigated states, and no new sharp reflections are observed during sodiation or desodiation. This indicates that Na storage in HC proceeds without a detectable long-range crystalline phase transformation. However, ex situ XRD cannot exclude local changes in interlayer spacing, defect sites, or nanopore filling.

The NFPP electrode retains its major crystalline diffraction features throughout charge and discharge (**Figure 8b**). Small changes in peak position, relative intensity, and broadening are observed as Na^+ is extracted and reinserted, indicating reversible lattice responses during cycling. The retention of the principal NFPP reflections suggests that the phosphate–pyrophosphate framework remains structurally intact and does not undergo a destructive phase transformation within the investigated voltage window.

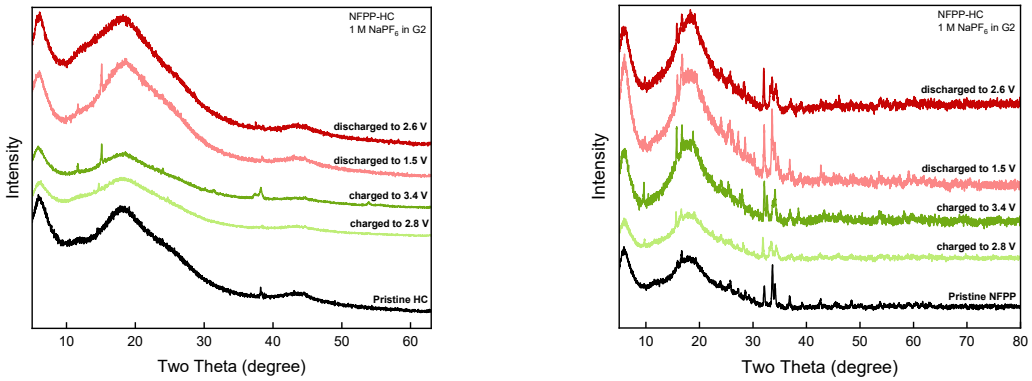


Figure 8 XRD patterns of (a) HC and (b) NFPP electrodes extracted from HC‖NFPP full cells at different charge and discharge voltages.

3.2 Electrochemical Investigation of NaPF_6/G2-Based Sodium-Ion Cells

According to **Figure 9a**, the first galvanostatic profiles of Na||HC half-cell showed that the additives strongly affected the first cycle charge balance. TPC produced the largest first-sodiation capacity, extending to approximately 460 mAh g^{-1}, substantially above the approximately 360 mAh g^{-1} obtained with BE. The corresponding desodiation capacity did not increase proportionally, leading to the lowest ICE. Therefore, TPC introduced a large irreversible first-sodiation contribution. This additional charge should not be assigned directly to increased Na storage in HC. It is more consistently interpreted as net sodium/electron consumption in additive reduction, electrolyte reduction, and interphase formation. TPC's fluorinated boron-containing structure provides a plausible basis for extensive formation of F/B-containing products. However, the specific products and their location cannot be determined from these curves alone. TTFPB also lowered ICE relative to BE, indicating additional first-cycle irreversible charge consumption. Because TTFPB contains sulfur-rich, sulfur–oxygen functionalities, sulfur containing decomposition products are plausible contributors to the interphase, but this remains to be chemically verified. TTFPB did not provide a clear first-cycle advantage over BE on HC. TMSPa gave an ICE of 84%, indicating it did not increase net irreversible sodium loss on HC during the first cycle. Its phosphate and trimethylsilyl groups may influence the initial interphase chemistry and may also scavenge reactive electrolyte species. Nevertheless, the ICE result alone does not prove formation of a thinner or more ionically conductive SEI. Based on **Figure 9b**, during cycling at 1C, BE showed the most stable HC capacity, remaining near 260 mAh g^{-1}. TPC exhibited the strongest fading, declining to approximately 225 mAh g^{-1}. On the other hand, TTFPB, TMSPa, and TTFPB + TMSPa also displayed gradual fading and did not clearly surpass BE. Therefore, under Na||HC half-cell conditions, none of the tested additives demonstrated a clearly more stable long-term HC interphase than BE. TPC was particularly detrimental because it combined high first-cycle irreversible loss with continuous capacity decay.

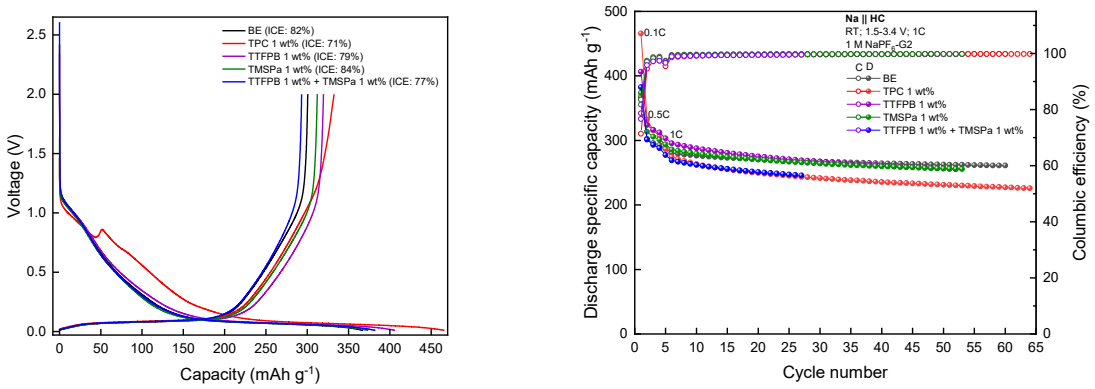


Figure 9 (a) Charge-Discharge profile and (b) discharge capacity and efficiency of HC half-cell.

The interpretation of the NFPP half-cell differs because the first step is charge, corresponding to Na extraction from NFPP rather than Na insertion into HC. From **Figure 10a**,TPC yielded an unusually large first-charge capacity, reaching approximately 170 mAh g^{-1}, whereas its first-discharge capacity was only about 80–85 mAh g^{-1}. Its ICE was therefore 55%, compared with 112% for BE, 111% for TTFPB, 114% for TMSPa, and 109% for TTFPB + TMSPa. This indicates that TPC induced a substantial irreversible charge contribution during the first oxidative process. Plausible processes include additive oxidation, electrolyte oxidation, and CEI formation at the NFPP surface. The high fluorine/boron content of TPC may be relevant to CEI chemistry, but the voltage profile does not establish which pathway dominates. Notably, after formation, TPC maintained a slightly higher discharge capacity than BE during NFPP cycling. Near the end of the test, TPC was approximately 83 mAh g^{-1}, compared with about 81–82 mAh g^{-1} for BE. This shows that the first-cycle TPC reaction was not purely detrimental to NFPP operation. One possible explanation is that TPC-derived products partially passivated the cathode and enabled access to slightly more reversible capacity. However, **Figure 10b** shows that the capacity still declined gradually, whereas BE remained nearly constant. TPC therefore increased post-formation capacity but did not improve the capacity retention of the NFPP half cell. TMSPa, TTFPB, and TTFPB + TMSPa showed first-cycle ICE values close to or above 100% and then near-100% Coulombic efficiency during subsequent cycling. Their discharge capacities nevertheless remained below BE or declined gradually. Values above 100% in the first cycle must be interpreted carefully. They indicate that the measured first discharge exceeded the measured first charge under the applied protocol, but they do not independently prove a superior CEI. The TMSPa structure is relevant because trimethylsilyl phosphate additives have been reported in related battery chemistries to affect interfacial stability and scavenge HF or fluorinated decomposition species. Such a role would be particularly relevant in $NaPF_6$-containing electrolytes.

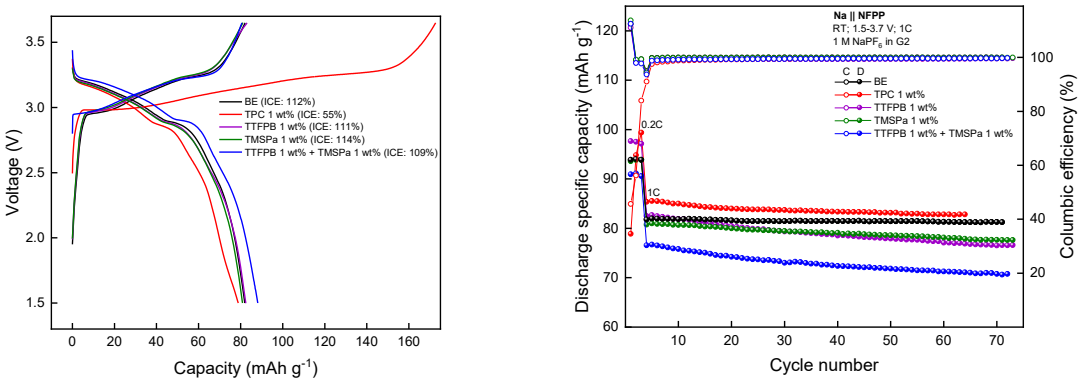


Figure 10 (a) Charge-Discharge profile and (b) discharge capacity and efficiency of NFPP half-cell.

The HC||NFPP full cell is the most meaningful test for practical electrolyte selection because it contains a finite sodium inventory. Sodium consumed irreversibly at HC or NFPP cannot be replenished by a large Na-metal reservoir. The performance therefore reflects the coupled stability of the HC SEI, NFPP CEI, bulk electrolyte, and sodium balance. **Figure 11 (a, b)** exhibits that BE gave an ICE of 86% and the most stable capacity, maintaining approximately 82–83 mAh g^{-1} through 100 cycles. The TMSPa formulation also showed an ICE of 86%. It delivered a higher initial discharge capacity than BE and gradually converged to approximately 83–84 mAh g^{-1} by cycle 100. Thus, TMSPa was the best-performing additive-containing formulation in the full cell and essentially preserved the performance of BE. This full-cell result is significant because TMSPa was not the top-performing formulation in either Na||HC or Na||NFPP half cells. A plausible explanation is that the chemistry of TMSPa is more favorable in the coupled HC||NFPP system than in cells employing Na metal. TMSPa may help control acidic/fluorinated species produced from $NaPF_6$/G2 and/or create more compatible interphases at the two practical electrodes. In a Na-metal half-cell, these potential benefits can be obscured by the highly reactive Na-metal interface, its own interphase formation, and the unlimited sodium reservoir. In contrast, TPC was unsuccessful in the full cell. TPC electrolyte gave an ICE of only 50% and its capacity decreased from approximately 70 mAh g^{-1} to around 35 mAh g^{-1} by cycle 100. The result is consistent with excessive irreversible sodium consumption in the complete cell. Although TPC gave slightly higher post-formation capacity in Na||NFPP, this cathode-side benefit could not compensate for sodium loss and/or interfacial degradation at HC in the sodium-limited full cell. The strongly fluorinated boron-containing molecular structure may promote interphase formation, but, at 1 wt% under the present conditions, the formation cost exceeded its benefit. The mixed additives confirmed the detrimental role of TPC-containing formulations under these conditions. The 0.5 wt% TPC + 0.5 wt% TMSPa formulation improved upon 1 wt% TPC, but still showed an ICE of 71% and decayed to approximately 73 mAh g^{-1}. The 0.5 wt% TPC + 0.5 wt% TTFPB formulation was the poorest overall, with an ICE of 34% and a final capacity below 50 mAh g^{-1}. The combination therefore did not produce an evident synergistic interphase. Instead, it increased irreversible sodium consumption.

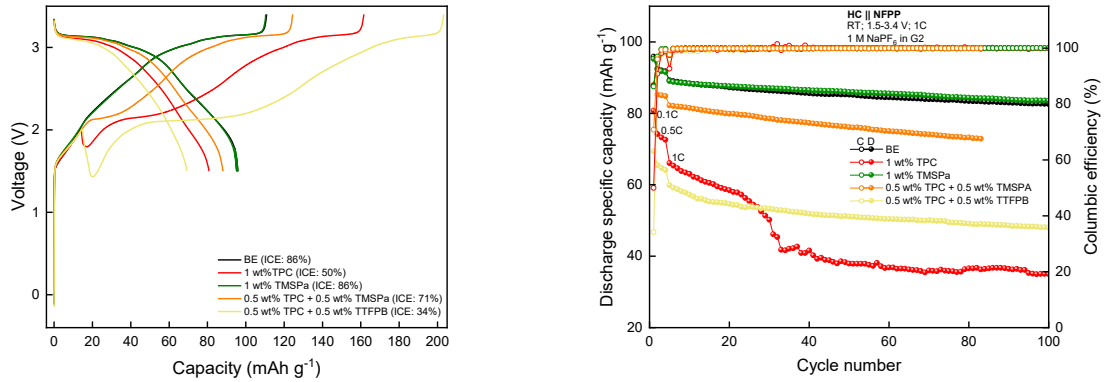


Figure 11 (a) Charge-Discharge profile and (b) discharge capacity and efficiency of HC||NFPP.

Based on **Figure 12 (a, b)**, temperature strongly affects the balance between reaction kinetics and interfacial stability in the additive-free HC||NFPP full cell. At 60°C, the improved ionic mobility and accelerated charge-transfer kinetics of the $NaPF_6$/G2 electrolyte lead to a more favorable initial electrochemical response compared with room temperature. However, the elevated temperature also accelerates reductive decomposition at the hard-carbon anode and oxidative decomposition at the NFPP cathode. These processes promote continuous SEI/CEI growth, consume cyclable sodium, and increase interfacial resistance. Consequently, although the high-temperature cell benefits from improved initial kinetics, it exhibits faster capacity fading during prolonged cycling.

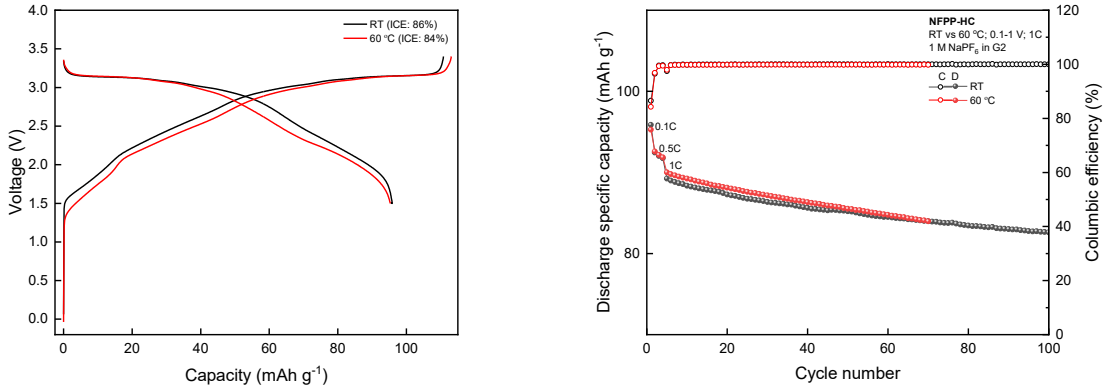


Figure 12 (a) Charge-Discharge profile and (b) discharge capacity and efficiency of HC||NFPP at different temperatures.

4. Conclusion

This study examined the effects of TPC, TTFPB, and TMSPa additives in a 1 M $NaPF_6$/diglyme (G2) electrolyte for Na-ion cells based on hard carbon (HC) and $Na_4Fe_3(PO_4)_2P_2O_7$ (NFPP). Solution-state ^{1}H and ^{23}Na NMR measurements showed that all additives modified the $NaPF_6$/G2 solvation environment, with TTFPB producing the largest apparent change in the average ^{23}Na resonance. This confirms that additive molecular structure affects Na^+–solvent/anion interactions; however, the magnitude of the bulk-solvation change alone did not predict electrochemical performance.

TPC caused substantial first-cycle irreversible charge consumption in both Na||HC and Na||NFPP half cells. Although it gave a slightly higher reversible capacity in the NFPP half cell after formation, it was detrimental in the sodium-limited HC||NFPP full cell, yielding a low initial Coulombic efficiency of 50% and severe capacity fading. TTFPB and TPC-containing mixed formulations likewise did not improve full-cell performance; the TPC/TTFPB mixture showed the lowest initial Coulombic efficiency, 34%. These findings show that any potential benefit associated with additive-induced changes in solvation or cathode-side behavior was outweighed by irreversible sodium consumption and/or unstable interfacial processes in the full cell.

Among the tested additive-containing electrolytes, 1 wt% TMSPa gave the most balanced full-cell response. It retained an initial Coulombic efficiency of 86%, identical to the baseline electrolyte, and maintained a capacity close to the baseline after 100 cycles. Nevertheless, the baseline electrolyte remained the most stable overall formulation under the investigated conditions. Ex situ XRD further showed that the broad turbostratic features of HC and the main crystalline reflections of NFPP were retained at the selected charged and discharged states, supporting structurally reversible sodium storage without a destructive long-range phase transformation. At 60°C, the baseline full cell exhibited a slightly lower initial Coulombic efficiency and faster capacity fading than at room temperature, indicating accelerated parasitic reactions and interfacial degradation at elevated temperature.

Overall, the results demonstrate that electrolyte-additive selection for HC||NFPP sodium-ion batteries must be based on full-cell sodium balance and long-term interfacial stability rather than half-cell capacity or solvation changes alone. TMSPa is the most promising additive candidate among those examined, while further optimization of its concentration and formation protocol, together with post-cycling interphase characterization, is required to establish a clear advantage over the baseline NaPF_6/G2 electrolyte.

ACKNOWLEDGEMENT

The author sincerely acknowledges Wandi Wahyudi for his valuable mentorship, guidance, and support throughout this project. The author also gratefully acknowledges Prof. Husam Alshareef for his supervision and for providing the research environment in which this work was conducted. This work was carried out at King Abdullah University of Science and Technology (KAUST), with support and funding from the KAUST Academy.

References

[1] P. Friedlingstein *et al.*, “Global Carbon Budget 2025,” *Earth Syst. Sci. Data*, vol. 18, no. 5, pp. 3211–3288, May 2026, doi: 10.5194/ESSD-18-3211-2026.

[2] M. Herrero-Gonzalez, N. El Arroubi, M. F. San-Roman, and R. Ibañez, “Acid−Base Flow Batteries for Sustainable Energy Storage: Balancing Energy Recovery and Efficiency,” *ACS Omega*, vol. 10, no. 48, p. 58420, Dec. 2025, doi: 10.1021/ACSOMEGA.5C06024.

[3] S. S. Gharehveran, K. Shirini, A. Abdolahi, S. S. Gharehveran, K. Shirini, and A. Abdolahi, “Optimizing Energy Storage Solutions for Grid Resilience: A Comprehensive Overview,” *Energy Storage Devices - A Comprehensive Overview*, Jan. 2025, doi: 10.5772/INTECHOPEN.1006499.

[4] M. H. Taabodi, T. Niknam, S. M. Sharifhosseini, H. Asadi Aghajari, and S. Shojaeiyan, “Electrochemical storage systems for renewable energy integration: A comprehensive review of battery technologies and grid-scale applications,” *J. Power Sources*, vol. 641, p. 236832, Jun. 2025, doi: 10.1016/J.JPOWSOUR.2025.236832.

[5] L. Song *et al.*, “Conquering self-discharge in supercapacitors: synergy of mechanisms and cross-scale mitigation strategies,” *J. Mater. Chem. A Mater.*, vol. 14, no. 21, pp. 12479–12508, Apr. 2026, doi: 10.1039/D5TA08045B.

[6] T. Sutikno[1] *et al.*, "Advanced energy storage technologies for renewable power systems: a comprehensive review," *Bulletin of Electrical Engineering and Informatics*, vol. 15, no. 4, pp. 3567–3586, Aug. 2026, doi: 10.11591/EEI.V15I4.4864.

[7] A. Yao, S. M. Benson, and W. C. Chueh, "Critically assessing sodium-ion technology roadmaps and scenarios for techno-economic competitiveness against lithium-ion batteries," *Nature Energy 2025 10:3*, vol. 10, no. 3, pp. 404–416, Jan. 2025, doi: 10.1038/s41560-024-01701-9.

[8] A. Yao, S. M. Benson, and W. C. Chueh, "Critically assessing sodium-ion technology roadmaps and scenarios for techno-economic competitiveness against lithium-ion batteries," *Nature Energy 2025 10:3*, vol. 10, no. 3, pp. 404–416, Jan. 2025, doi: 10.1038/s41560-024-01701-9.

[9] E. O. Eren *et al.*, "Hard carbon from a sugar derivative for next-generation sodium-ion batteries," *Mater. Horiz.*, vol. 12, no. 3, pp. 886–898, Feb. 2025, doi: 10.1039/D4MH01118J.

[10] C. Wu *et al.*, "Hard carbon for sodium-ion batteries: progress, strategies and future perspective," *Chem. Sci.*, vol. 15, no. 17, pp. 6244–6268, May 2024, doi: 10.1039/D4SC00734D.

[11] A. Rehman, S. Saleem, S. Ali, S. M. Abbas, M. Choi, and W. Choi, "Recent advances in alloying anode materials for sodium-ion batteries: material design and prospects," *Energy Materials*, vol. 4, no. 6, p. 400068, Dec. 2024, doi: 10.20517/ENERGYMATER.2024.06.

[12] Z. Lu *et al.*, "Consummating ion desolvation in hard carbon anodes for reversible sodium storage," *Nature Communications 2024 15:1*, vol. 15, no. 1, pp. 3497-, Apr. 2024, doi: 10.1038/s41467-024-47522-y.

[13] A. F. Abdul Salam *et al.*, "Sodium-ion battery development since 2020 with future perspectives," *J. Mater. Chem. A Mater.*, vol. 14, no. 16, pp. 9115–9137, Mar. 2026, doi: 10.1039/D5TA07726E.

[14] C. R. Lee *et al.*, "Vulnerable Solid Electrolyte Interphase Deposition in Sodium-Ion Batteries from Insufficient Overpotential Development during Formation," *ACS Mater. Lett.*, vol. 6, no. 3, pp. 772–779, Mar. 2024, doi: 10.1021/ACSMATERIALSLETT.3C01616.

[15] R. Li *et al.*, "Low-temperature sodium-ion batteries: challenges, engineering strategies, safety considerations, and future directions," *EES Batteries*, vol. 1, no. 6, pp. 1444–1480, Dec. 2025, doi: 10.1039/D5EB00121H.

[16] H. Qu, W. Hu, Y. Huang, T. Zhang, H. Fang, and F. Li, "Recent Advances and Practical Challenges in Organic Electrolytes of Sodium-Ion Batteries," *Energy & Fuels*, vol. 38, no. 14, pp. 12472–12486, Jul. 2024, doi: 10.1021/ACS.ENERGYFUELS.4C01974.

[17] F. Cheng *et al.*, "Reviving ether-based electrolytes for sodium-ion batteries," *Energy Environ. Sci.*, vol. 18, no. 14, pp. 6874–6898, Jul. 2025, doi: 10.1039/D5EE00725A.